LAWRENCE LIVERMORE NATIONAL LABORATORY

LLNL-TR-869706

Adjoint waveform tomography of East Asia for improved waveform prediction

C. Doody, N. Simmons, A. Rodgers

September 26, 2024

This work performed under the auspices of the U.S. Department of Energy by Lawrence Livermore National Laboratory under Contract DE-AC52-07NA27344.

Lawrence Livermore National Laboratory

Technical Report on Adjoint Waveform Tomography of East Asia for Improved Waveform Prediction

Claire Doody, Nathan Simmons, Artie Rodgers

September 26, 2024

This Ground-based Nuclear Detonation Detection (GNDD) research was funded by the National Nuclear Security Administration, Defense Nuclear Nonproliferation Research and Development (NNSA DNN R&D). Lawrence Livermore National Laboratory is operated by Lawrence Livermore National Security, LLC, for the U.S. Department of Energy, National Nuclear Security Administration under Contract DE-AC52-07NA27344. LLNL-TR-869706

Abstract

We present a preliminary version of the East Asia Tomography (EAT) model, an adjoint waveform tomography model of East and Southeast Asia. We used SPiRaL (Simmons et al., 2021) as our starting model and source parameters for 238 earthquakes from the Global Centroid Moment Tensor catalogue (Ekström et al., 2012). After 50 iterations on Lawrence Livermore National Laboratory's Lassen supercomputer, we converge on a model with a minimum period of 50 seconds. The preliminary model shows improved slab structure compared to SPiRaL and shows significantly reduced misfit. In later versions of the model, we aim to harness techniques proposed in other studies to improve waveform predictions that travel through the ocean (e.g., Wehner et al., 2022) and use relative amplitude-based misfit functions (e.g., Tao et al., 2018) to better constrain Earth structure. We hope to iterate the current extent of the model to 25 seconds minimum period before iterating to shorter periods for a smaller subregion of the full model.

Introduction

The Eurasian continent is a heavily studied region in seismic tomography due to the complex tectonic processes that have shaped the region. East Asia hosts numerous subduction zones along the Ring of Fire, spanning from the Kamchatka Peninsula in northeastern Russia to the Philippine Islands near the Equator. In central Eurasia, the Indian subcontinent collides with southwestern China, creating the Himalaya Mountains and the extrusion of the Tibetan Plateau to the east. Intraplate volcanism in northeastern China has debated origins in the deep mantle or from deep dehydration of the subducted Pacific Slab. These features and more have led to extensive imaging studies of Eurasia.

While traditional imaging studies have used body wave tomography (e.g., Fu et al., 2023; Fukao and Obayashi, 2013) and surface wave tomography (e.g., Li et al., 2013; Li et al., 2022; Liu and Zhao, 2016; Yang et al., 2021), recent imaging studies of East Asia have focused on using adjoint waveform tomography (AWT) to produce detailed models of the region (e.g., Liu et al., 2024; Ma et al., 2022; Simute et al., 2016; Tao et al., 2018; Xi et al., 2024). Compared to traditional techniques, AWT uses more of the seismic waveform by windowing data around certain phases (e.g., Xi et al., 2024) or by windowing based on similarity between the observed and synthetic data (e.g., Ma et al., 2022). AWT methods have been shown to improve waveform predictions over traditional models (Rodgers et al., 2022) and produce more defined subsurface features, particularly of subducting slabs (Rodgers et al., 2024).

In this preliminary study, we present a long period model of greater East and Southeast Asia. Even at long periods, we see improvement in slab structure compared to SPiRaL, our starting model, and reduce the misfit by 45% over 50 iterations. As we begin including shorter period information, we aim to harness methodological advances of recent studies to improve subsurface structure by considering relative amplitudes in our misfit function and to simulate seismic waves through the ocean layer. Though these choices increase computational expense, we hope that they will improve both waveform predictions and subsurface structure.

Data

Because of its tectonic complexity, East Asia experiences significant moderate-magnitude seismicity. The Global Centroid Moment Tensor (GCMT) Catalogue (Dziewonski et al., 1981; Ekström et al., 2012), a global moment tensor catalogue for events over Mw 5 includes over

2400 events between Mw5.0-7.0 between 1 January 2010 and 31 March 2021. Because using all available events is infeasible, we spatially binned the available events. We used bins that are 100 km by 100 km laterally and 25 km in depth. Because events are scarce in the deep Earth, we included all events with depths greater than 500 km. Binning the events reduced the number of events to around 600. We simulated data for all binned events and picked windows for all events using a modified version of the FLEXWIN algorithm (Maggi et al., 2009). If an event had less than 20 stations contributing data or if less than 40% of stations contributed windows to an event, they were removed from the dataset due to their limited data or poor data quality. After quality control, we converged on a final dataset of 238 events (Figure 1). Data is downloaded from the EarthScope Data Management Center using the Obspy MassDownloader tool. Around 800 stations from both permanent and temporary networks contributed data to the inversions.

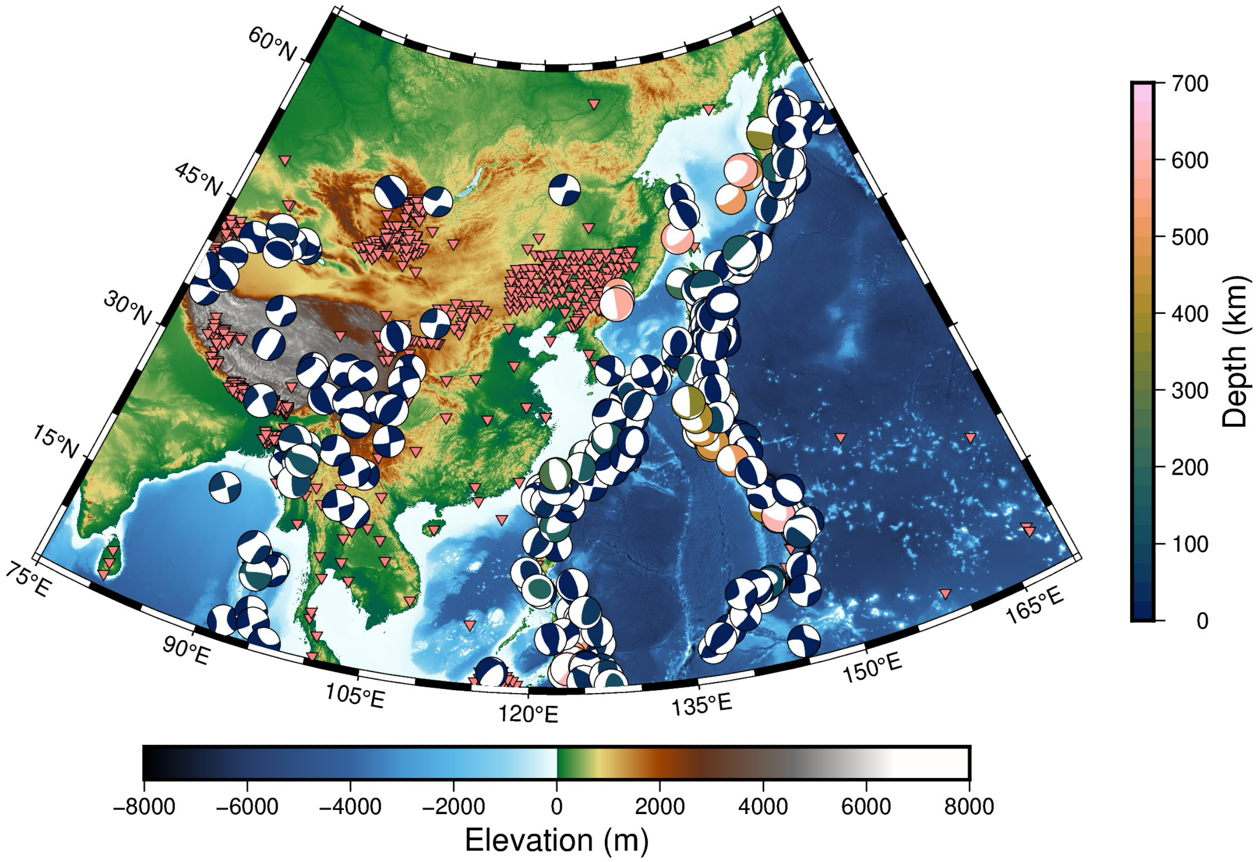

Figure 1. Map of the 238 events used in the construction of the EAT model. Moment tensors are taken from the Global Centroid Moment Tensor (GCMT) catalogue and are colored by the depth of the event. Red triangles represent seismic stations used in the inversion of the EAT model.

Methods

We used Salvus (Afanasiev et al., 2019) to run inversions of the EAT model. Forward simulations are run using the spectral element method (Komatitsch & Tromp, 1999; Komatitsch & Vilotte, 1998). Simulations were run on Lawrence Livermore National Laboratory's Lassen high-performance computing system on four NVIDIA Tesla V100 GPUs. After we calculated synthetics, we picked windows using a modified version of the FLEXWIN algorithm (Maggi et al., 2009) proposed in Krischer et al. (2015). Windows were not restricted to given phases; instead, data were windowed based on a variety of constraints on the similarity between the observed and synthetic data (see Doody et al., 2023a for a detailed description). After window picking, we weighted windows based on the event-dependent station weighting scheme from Ruan et al. (2019). Station weights were calculated based on distance from the source and station density in a given region (i.e., clustered stations are downweighted while isolated stations are upweighted).

We calculated the misfit between the observed and synthetic data using the time-frequency phase misfit function (Fichtner et al., 2008). The time-frequency phase misfit function first transforms the time domain data into the time-frequency domain (Kristeková et al., 2006, 2009) then calculates the weighted phase difference and envelope similarity. The time-frequency phase misfit function is a phase-based misfit function, so relative amplitudes are not included in the calculation of the misfit. We then computed sensitivity kernels for each event based on the interaction of the forward and adjoint wavefields. The sensitivity kernels were smoothed anisotropically, with 0.5 wavelength smoothing laterally and 0.2 wavelength smoothing vertically. The smoothing length was chosen by Vsv wavelengths. To minimize source and receiver effects, we set kernel values to zero around sources and receivers. The source/receiver cutouts are spherical with 300 km and 75 km radii respectively.

Model updates were computed using the trust-region Limited-memory Broyden-Fletcher-Goldfarb-Shanno (L-BFGS) algorithm, which is a quasi-Newton optimization algorithm (e.g., Conn et al., 2000; Nocedal and Wright, 2006). L-BFGS methods, and the trust-region L-BFGS method particularly, provide significant computational speed-up over conjugate gradient methods (Modrak and Tromp, 2016; Thrastarson et al., 2021). We used the trust-region L-BFGS method of Boehm et al. (2018), which solves an auxillary optimization problem to minimize the quadratic approximation of the misfit surface. In this approach, the size of model updates are constrained by the ratio between the predicted and actual misfit reduction of a given model update. Alignment between the predicted and actual misfit reductions allows us to make many model updates and avoid being trapped in local minima. We iterated on the model until the misfits could no longer be reduced; after an iteration failed to reduce the misfit with two target models, we ended the iteration stage.

Discussion

The model presented below is a preliminary model of East Asia, iterated to a minimum period of 50 seconds. At the 50-150 second period band, we iterated on the model 50 times. The misfit was reduced by 45% across all 50 iterations (Figure 2). While 30% of the misfit is reduced in the first 8 stages, continuing to iterate on the model significantly reduces the misfit over the remaining 42 iterations. Previous studies have highlighted the importance of running many iterations to make it less likely that the model will converge to a local minimum (e.g., Rodgers et al., 2024).

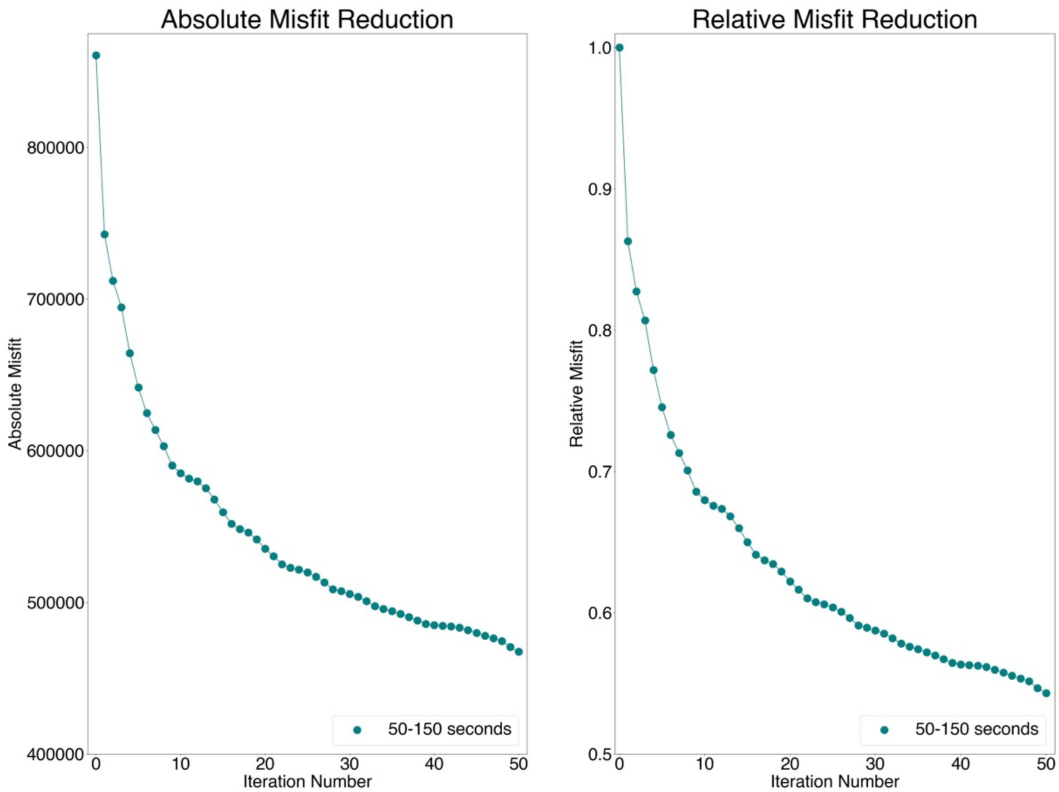

Figure 2. Absolute and relative time-frequency phase misfit reduction over 50 iterations in the 50-120s period band.

As for the preliminary EAT model, Figure 3 shows the model after 50 iterations compared to its starting model, SPiRaL. Compared to SPiRaL, EAT shows higher-amplitude slab features in the upper- to mid-mantle depths (150-600 km). The third column shows the natural log of the ratio between the two models. The natural log shows the spatial pattern of the updates; the values represent the amplitude of the changes to absolute velocities. Sharp boundaries in the upper mantle (Figures 3a-b) and the mid-mantle (Figures 3g-h) represent the Moho and the 410 km boundary, respectively. We honored Moho topography from Crust1.0 (Laske et al., 2013) and 410 km and 660 km topography from Lawrence and Shearer (2008). The subducting Pacific Slab underneath eastern Russia is low-amplitude in SPiRaL (Figure 3g), making it appear as if the slab is discontinuous between the Kamchatka Peninsula and Hokkaido, Japan. In EAT, by contrast, the Pacific Slab appears continuous in this region (Figure 3h). At 600 km, the stagnant Pacific Slab is visible in both models underneath northern China; the slab is higher amplitude in the EAT model (Figure 3k) and has faster amplitudes below the Chiangbaishan intraplate volcano. Further iterations at shorter periods will better constrain slab structure, so we reserve any tectonic interpretation for the final model.

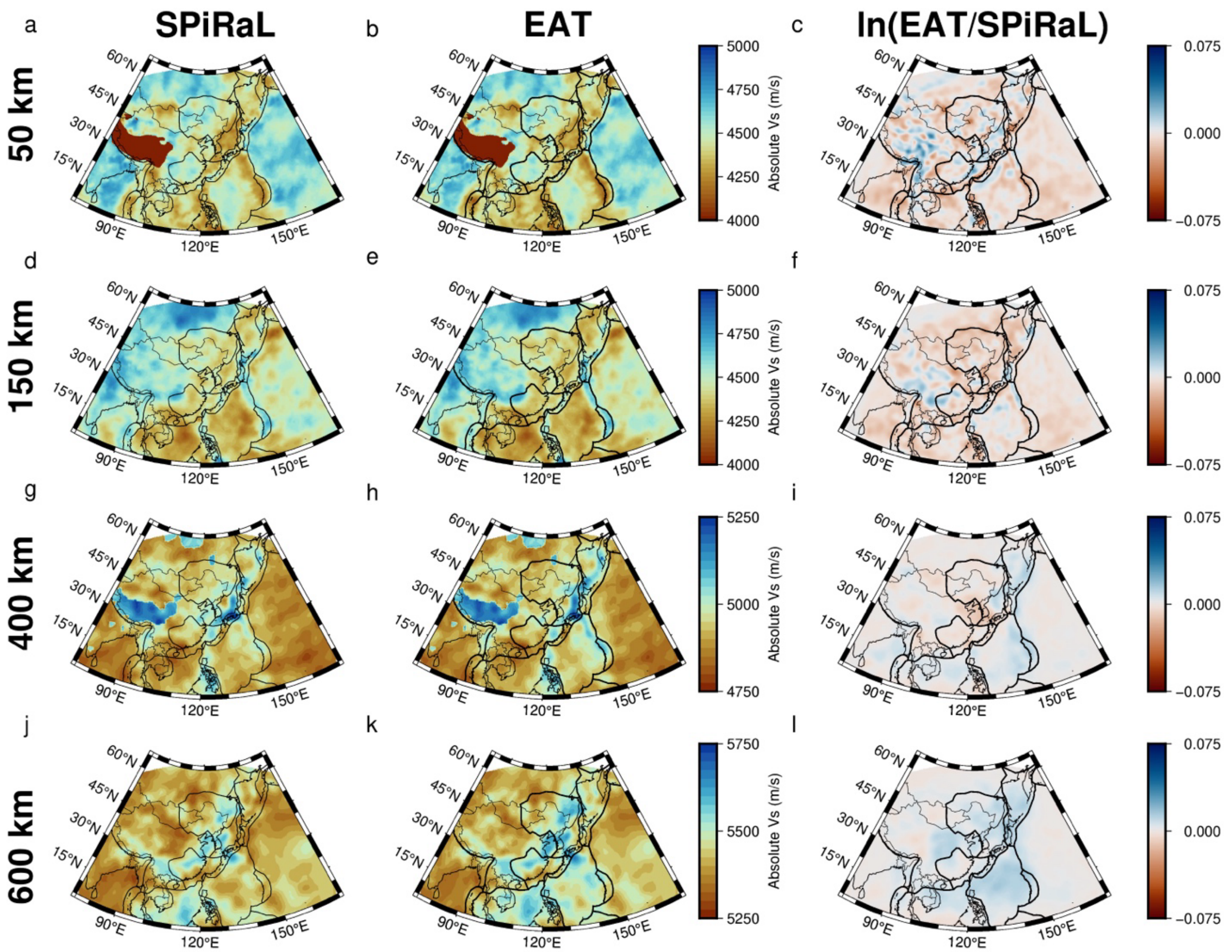

Figure 3. Map view comparisons of SPiRaL (Simmons et al., 2021) and the EAT model after 50 iterations. Voigt-averaged isotropic V_S values for the SPiRaL model are plotted in the leftcolumn and V_S values for the preliminary EAT model are plotted in the middle column. The color scale is the same for the two models. The right column shows the natural log between the ratio of the two

models. The blue regions show areas where the V_S of the EAT model is faster than SPiRaL; red regions show areas where the V_S of the EAT model is slower than SPiRaL.

To refine the structure of the model, we plan to follow a multi-scale approach and iteratively lower the minimum period to resolve smaller scale features. We aim to reach a minimum period of 25 seconds. On top of lowering the minimum period, we also plan to change to a misfit function that considers relative amplitudes (e.g., Tao et al., 2017, 2018) once we begin iterating below 30 seconds. Considering relative amplitudes on top of phase will improve waveform predictions and provide more accurate constraints on mantle structure. Finally, we plan to couple acoustic and elastic simulations to simulate waves propagating through the ocean layer to improve waveform predictions. Traditional spectral-element simulations use an ocean loading approximation (Komatitsch and Tromp, 2002b), which holds at long periods but breaks down at shorter periods (Fernando et al., 2020; Wehner et al., 2022). A large portion of our domain covers the Pacific Ocean and accurately modelling the effect of the oceans on waveforms from stations on Pacific Islands will improve our ability to predict short-period waveforms.

Conclusions

We present a preliminary version of the East Asian Tomography (EAT) model, an adjoint waveform tomography model of greater East Asia. The EAT model used SPiRaL (Simmons et al., 2021) as a starting model and used data from nearly 240 events recorded at over 800 permanent and temporary seismic stations. We ran 50 iterations at 50-150 second period band and achieved a 45% reduction in misfit compared to SPiRaL. The preliminary EAT model shows improved slab structure in the mid-mantle compared to SPiRaL, though we reserve any tectonic interpretation for future work. To further improve the model, we plan on: 1. Iterating at shorter periods using a multi-scale approach, 2. Introducing a relative-amplitude-based misfit function (Tao et al., 2018), and 3. Modelling wave propagation through the ocean layer to further improve waveform predictions.

References

Afanasiev, M., Boehm, C., Van Driel, M., Krischer, L., Rietmann, M., May, D. A., et al. (2019). Modular and flexible spectral-element waveform modelling in two and three dimensions. *Geophysical Journal International*, **216(3)**, 1675–1692. https://doi.org/10.1093/gji/ggy469

Boehm, C., Korta Martiartu, N., Jovanović Balic, I., Fichtner, A., & Vinard, N. (2018). Time-domain spectral-element ultrasound waveform tomography using a stochastic quasi-Newton method. https://doi.org/10.1117/12.2293299

Conn, A. R., Gould, N. I. M., & Toint, P. L. (2000). Trust region methods. SIAM-MPS.

Doody, C. D., Rodgers, A. J., Afanasiev, M., Boehm, C. T., Krischer, L., Chiang, A., & Simmons, N. (2023a). Comparing adjoint waveform model of California using different starting models. *Journal of Geophysical Research: Solid Earth*, **128(5)**. https://doi.org/10.1029/2023jb026463

Dziewonski, A. M., Chou, T. A., & Woodhouse, J. H. (1981). Determination of earthquake source parameters from waveform data for studies of global and regional seismicity. *Journal of Geophysical Research*, **86(B4)**, 2825–2852. https://doi.org/10.1029/JB086iB04p02825

Ekström, G., Nettles, M., & Dziewoński, A. M. (2012). The global CMT project 2004-2010: Centroid-moment tensors for 13,017 earthquakes. *Physics of the Earth and Planetary Interiors*, **200–201**, 200–209. https://doi.org/10.1016/j.pepi.2012.04.002

Fernando, B., Leng, K., & Niseen-Meyer, T. (2020). Oceanic high-frequency global seismic wave propagation with realistic bathymetry. *Geophysical Journal International*, **222(2)**, 1178-1194. https://doi.org/10.1093/gji/ggaa248

Fichtner, A., Kennett, B. L. N., Igel, H., & Bunge, H. P. (2008). Theoretical background for continental- and global-scale full-waveform inversion in the time-frequency domain. *Geophysical Journal International*, **175(2)**, 665–685. https://doi.org/10.1111/j.1365-246X.2008.03923.x

Fu, Y., Wang, Z., & Obayashi, M. (2023). Global P-wave and joint S-wave tomographyin the North Pacific: Implications for slab geometry and evolution. *Journal of Geophysical Research: Solid Earth*, **128(11)**. https://doi.org/10.1029/2023JB027406

Fukao, Y., & Obayashi, M. (2013). Subducted slabs stagnant above, penetrating, and trapped below the 660 km discontinuity. *Journal of Geophysical Research: Solid Earth*, **118(11)**, 5920-5938. https://doi.org/10.1002/2013JB010466

Komatitsch, D., & Tromp, J. (1999). Introduction to the spectral element method for three-dimensional seismic wave propagation. *Geophysical Journal International*, **139(3)**, 806–822. https://doi.org/10.1046/j.1365-246x.1999.00967.x

Komatitsch, D., & Tromp, J. (2002b). Spectral-elementsimulations of global seismic wave propagation—II. Three-dimensional models, oceans, rotation, and self-gravitation. *Geophysical Jounral International*, **150(1)**, 303-318. https://doi.org/10.1046/j.1365-246X.2002.01716.x

Komatitsch, D., & Vilotte, J.-P. (1998). The spectral element method: An efficient tool to simulate the seismic response of 2D and 3D geological structures. *Bulletin of the Seismological Society of America*, **88(2)**, 368–392. https://doi.org/10.1785/BSSA0880020368

Krischer, L., Fichtner, A., Zukauskaite, S., & Igel, H. (2015). Large-scale seismic inversion framework. *Seismological Research Letters*, **86(4)**,1198–1207. https://doi.org/10.1785/0220140248

Kristeková, M., Kristek, J., & Moczo, P. (2009). Time-frequency misfit and goodness-of-fit criteria for quantitative comparison of time signals. *Geophysical Journal International*, **178(2)**, 813–825. https://doi.org/10.1111/j.1365-246X.2009.04177.x

Kristeková, M., Kristek, J., Moczo, P., & Day, S. M. (2006). Misfit criteria for quantitative comparison of seismograms. *Bulletin of the Seismological Society of America*, **96(5)**, 1836–1850. https://doi.org/10.1785/0120060012

Laske, G., Masters, G., Ma, Z., & Pasyanos, M. (2013). Update on CRUST1.0- a 1-degree global model of Earth’s crust. *Geophysical Research Abstracts*, **15**, Abstract EGU2013-2658.

Lawrence, J. F., & Shearer, P. M. (2008). Imaging mantle transition zone thickness with *SdS-SS* finite-frequency sensitivity kernels. *Geophysical Journal International*, **174(1)**, 143-158. https://doi.org/10.1111/j.1365-246X.2007.03673.x

Li, M., Song, X., Li, J., & Bao, X. (2022). Crust and upper mantle structure of East Asia from ambient noise and earthquake surface wave tomography. *Earthquake Science*, **35(2)**, 71-92. https://doi.org/10.1016/j.eqs.2022.05.004

Li, Y., Wu, Q., Pan, J., Zhang, F., & Yu, D. (2013). An upper mantle S-wave velocity model of East Asia from Rayleigh wave tomography. *Earth and Planetary Science Letters*, **337-338**, 367-377. https://doi.org/10.1016/j.epsl.2013.06.033

Liu, C., Banerjee, R., Grand, S. P., Sandoval, E., Mitra, S., Liang, X. & Wei, S. (2024). A high-resolution seismic velocity model of East Asia using full-waveform tomography: Constraints on India-Asia collisional tectonics. *Earth and Planetary Science Letters*, **639**. https://doi.org/10.1016/j.epsl.2024.118764

Liu, X., & Zhao, D. (2016). Backarc spreading and mantle wedge flow beneath the Japan Sea: Insights from Rayleigh-wave anisotropic tomography. *Geophysical Journal International*, **207(1)**, 357-373. https://doi.org/10.1093/gji/ggw288

Ma, J., Bunge, H.-P., Thrastarson, S., Fichtner, A., van Herwaarden, D.-P., Tian, Y., Chang, S.-J., & Liu, T. (2022). Seismic full-waveform inversion of the crust-mantle structure beneath China and adjacent regions. *Journal of Geophysical Research: Solid Earth*, **127(9)**. https://doi.org/10.1029/2022JB024957

Maggi, A., Tape, C., Chen, M., Chao, D., & Tromp, J. (2009). An automated time-window selection algorithm for seismic tomography. *Geophysical Journal International*, **178(1)**, 257-281. https://doi.org/10.1111/j.1365-246X.2009.04099.x

Modrak, R., & Tromp, J. (2016). Seismic waveform inversion best practices: Regional, global and exploration test cases. *Geophysical Journal International*, **206(3)**, 1864–1889. https://doi.org/10.1093/gji/ggw202

Nocedal, J., & Wright, S. (2006). Numerical optimization. Springer.

Rodgers, A., Doody, C., & Fichtner, A. (2024). WUS324: Full waveform inversion approaching convergence improves waveform fits while imaging seismic structure of the Western United States. *Geophysical Research Letters*, in revision.

Rodgers, A., Krischer, L., Afanasiev, M., Boehm, C., Doody, C., Chiang, A., & Simmons, N. (2022). WUS256: An adjoint waveform tomography model of the crust and upper mantle of the western United States for improved waveform simulations. *Journal of Geophysical Research: Solid Earth*, **127(7)**. https://doi.org/10.1029/2022JB024549

Ruan, Y., Lei, W., Modrak, R., Örsvuran, R., Bozdag, E., & Tromp, J. (2019). Balancing unevenly distributed data in seismic tomography: A global adjoint tomography example. *Geophysical Journal International*, **219(2)**, 1225–1236. https://doi.org/10.1093/gji/ggz356

Simmons, N. A., Myers, S. C., Morency, C., Chiang, A., & Knapp, D. R. (2021). SPiRaL: A multi-resolution global tomography model of seismic wave speeds and radial anisotrophy variations in the crust and mantle. *Geophysical Journal International*, **227(2)**, 1366–1391. https://doi.org/10.1093/gji/ggab277

Simutè, S., Steptoe, H., Cobden, L., Gokhberg, A., & Fichtner, A. (2016). Full-waveform inversion of the Japanese Islands. *Journal of Geophysical Research: Solid Earth*, **121(5)**, 3722-3741. https://doi.org/10.1002/2016JB012802

Tao, K., Grand, S. P., & Niu, F. (2017). Full-waveform inversion of triplicated data using a normalized-correlation-coefficient-based misfit function. *Geophysical Journal International*, **210**, 1517-1524. https://doi.org/10.1093/gji/ggx249

Tao, K. Grand, S. P., & Niu, F. (2018). Seismic structure of the uppder mantle beneath Eastern Asia from full waveform seismic tomography. *Geochemistry, Geophysics, Geosystems*, **19(8)**, 2732-2763. https://doi.org/10.1029/2018GC007460

Thrastarson, S., Van Herwaarden, D., & Fichtner, A. (2021). Inversions on: Fully automated seismic waveform inversions. *EarthArXiv*. https://doi.org/10.31223/X5F31V

Wehner, D., Rawlinson, N., Greenfield, T., Daryono, M. S., Supendi, P., ChuanChuan, L., & Widiyantoro, S. (2022). SASSIER22: Full-waveform tomography of the eastern Indonesian region that includes topography, bathymetry, and the fluid ocean. *Geochemistry, Geophysics, Geosystems*, **23(11)**. https://doi.org/10.1029/2022GC010563

Xi, Z., Chen, M., Wei, S., Li, J., Zhou, T., Wang, B., & Kim, Y. (2024). EARA2024: A new radially anisotropic seismic velocity model for the crust and upper mantle beneath East Asia and Northwestern Pacific subduction zones. *Geophysical Journal International*. https://doi.org/10.1093/gji/ggae302

Yang, X., Luo, Y., & Zhao, K. (2021). 3D crustal and upper mantle model of East Asia from a joint inversion of surface and body waves and its tectonic implications. *Journal of Geophysical Research: Solid Earth*, **126(12)**. https://doi.org/10.1029/2021JB022667